# X-ray scattering and atomic force microscopy study of melting of Langmuir-Blodgett films

J. K. Basu, M. K. Sanyal, M. Mukherjee, and S. Banerjee

*Surface Physics Division, Saha Institute of Nuclear Physics, 1/AF, Bidhannagar, Calcutta 700 064, India*
(Received 29 February 2000)

Melting of 9-ML cadmium arachidate Langmuir-Blodgett (LB) films, having logarithmic and self-affine interfacial height-height correlations, has been studied by x-ray specular reflectivity, diffuse scattering, and atomic force microscopy (AFM). Although analysis of AFM images and diffuse scattering data for both films indicates that the respective in-plane correlation of the untreated films remains unchanged up to 100 °C it is evident from analysis of the diffuse integrated reflectivity data that a reduction of electron density at metal sites occurs as a function of temperature. Between 100 and 110 °C the film disorders completely and the bilayer structure breaks down. A systematic analysis of x-ray and AFM data suggest that a disordering prior to the melting of LB films takes place predominantly via lateral motion of molecules, keeping the interfacial correlation unchanged irrespective of the interfacial morphology of the untreated film.

## I. INTRODUCTION

Langmuir monolayers are quasi-two-dimensional (2D) systems that are formed simply by spreading amphiphillic molecules, consisting of polar and nonpolar parts, on water.[1,2] These monolayer films on water exhibit a rich variety of exotic phases as a function of pressure and temperature. Much of theoretical[3] and experimental[4,5] work has been done to understand the structure and thermodynamics of monolayer films of some prototypical molecules. Using the Langmuir-Blodgett (LB) technique, ordered multilayer films of amphillic molecules can be deposited by a relatively unsophisticated technique[6] of repeated dipping of a solid substrate through a Langmuir monolayer. As a result Langmuir monolayers and LB films are ideal systems to study the effect of reduced dimensions on physical properties. Although it was known that these LB films have a well-ordered structure along the growth direction (the $z$ direction), the growth mechanism and the dependence of the structure of the Langmuir monolayer and of various deposition parameters like dipping speed, film-substrate interaction, etc. on the quality of the deposited film is not very well understood.[6,7] Recently some work was done to understand the in-plane structure of these films,[8–12] which shed some light onto their growth mechanism.[12]

In comparison, not much work has been done to understand the melting process of deposited LB films. A study of the melting of multilayer LB films, having few monolayers, should be quite interesting, since these quasi-2D systems are expected to follow predictions for melting of 2D solids.[13] In some earlier works,[14] it was shown that melting in LB films proceeds via a disordering transition followed by a melting transition at a much higher temperature. An electron-diffraction study[15] on monolayers of cadmium stearate, arachidate and behenate, indicated that the monolayer melts to a liquid state through an intermediate hexaticlike phase, although the exact mechanism of disordering could not be determined. From high-resolution x-ray-diffraction studies, it was interpreted that thermal melting of arachidic acid monolayers occurred via a two-step process consisting of a slowly evolving continuous untilting of initially tilted chains, and then finally chain melting due to the onset of gauche disorders resulting in the formation of kinks and jogs along the chains.[16] Results of some recent experiments[17] on LB films seem to match earlier theoretical predictions on the melting of anisotropic 2D crystals,[18] which proceeds via an additional intermediate phase as compared to melting of isotropic 2D solids. Using a combination of *in situ* grazing-incidence x-ray specular reflectivity and diffuse scattering and *ex situ* atomic face microscopy (AFM), here we try to understand the complex mechanism of melting and its dependence on the interfacial morphology in LB films.

Grazing-incidence x-ray reflectivity and diffuse scattering are powerful techniques for nondestructive probing of the structure of surface and interfaces. X-ray specular reflectivity measurements provide information about the interfacial roughnesses, thicknesses, and average electron densities of different sublayers of a thin film.[19–21] X-ray off-specular diffuse scattering, on the other hand, provide an understanding of the lateral correlation in and between rough interfaces; in particular, it gives height-height correlation functions for the interfaces.[20–22] Although a calculation of diffuse scattering from multilayer systems was performed recently, analysis of diffuse scattering data becomes convenient if the system has conformal or correlated roughness.[23] Multilayer LB films have been found to show a remarkable degree of correlation[8–12] between interfaces, so that an analysis of diffuse scattering data from these systems can generally be based on the assumption of conformal interfaces.

AFM recently emerged as a very powerful structural probe, giving information in real space, for practically all types of surfaces, especially for soft materials like organic films.[24] In addition to atomic resolution images of surfaces one can obtain, with AFM, a quantitative morphological information even up to a micron length scale. For instance, it is possible to measure the local rms roughness of a surface by performing scans of different lengths. From the scaling of this measured local roughness with scan size, it is possible to extract the roughness exponent.[12,25] Although AFM measurements are restricted to the top surface only, they provide
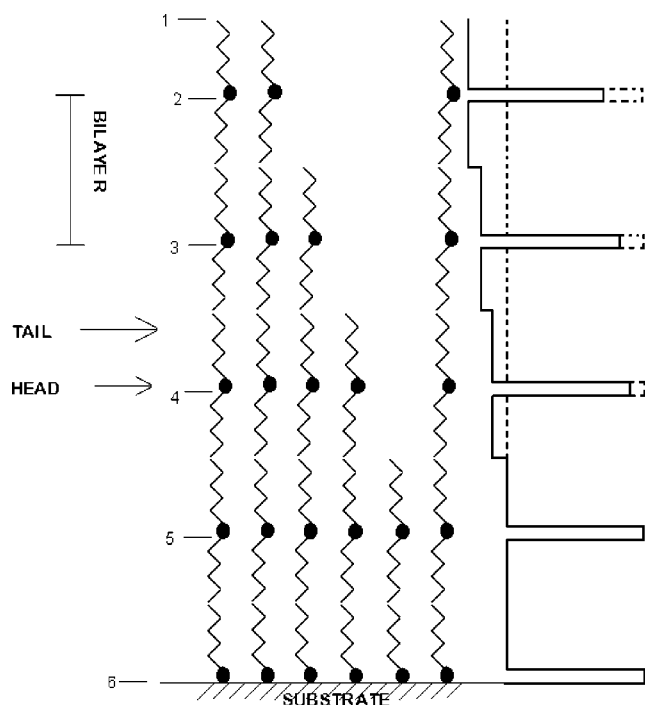
FIG. 1. Schematic of a LB film deposited on a hydrophillic substrate. The interfaces have been labeled as shown. The dashed line shown alongside is the EDP for an ideal film structure, while the solid line shows a disordered structure indicated by missing molecules in the top three bilayers.
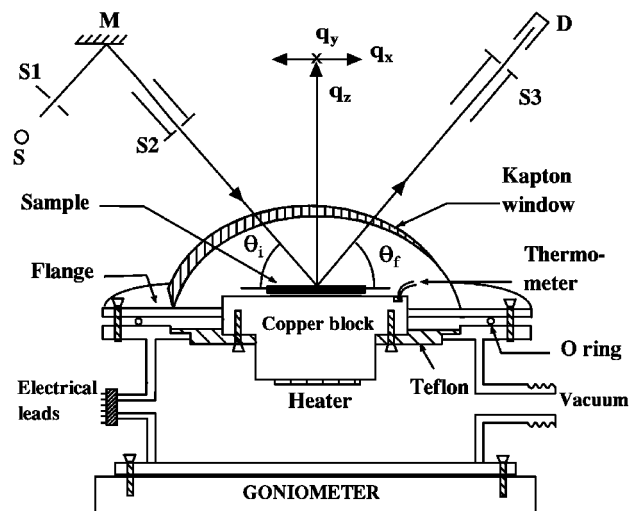


FIG. 2. Schematic of the experimental setup (side view) used to perform *in situ* measurements of x-ray reflectivity data at different temperatures. $S$ is the rotating Cu anode, $D$ is the detector, $M$ is the monochromator [Si (111) crystal face], $S1$ is a variable aperture slit, and $S2$ and $S3$ are slits with fixed apertures. The scattering geometry is also indicated. A specular scan is performed along the $q_z$ axis, with $q_x=0$, while a longitudinal off-specular scan is performed along the $q_z$ direction but at a nonzero $q_x$ value. A transverse diffuse scan is performed along the $q_x$ direction at a fixed nonzero $q_z$ value. All these scans are performed at about $q_y=0$.

information complementary to that obtained from x-ray scattering measurements.

In Sec. II we first discuss the experimental details of deposition of our LB film and then describe our experimental setup for performing x-ray specular reflectivity and diffuse scattering experiments, including the sample cell used for *in situ* high-temperature measurements; the details of AFM measurements are also provided in this section. In Sec. III we give the theoretical background for a mathematical description of surface morphology, and outline the formalism for scattering of x rays from rough surfaces. We then discuss the results of x-ray scattering and AFM data, and finally discuss the mechanism of melting of the LB film.

## II. EXPERIMENTAL DETAILS

Here we have investigated melting of 9-ML cadmium arachidate (CdA) LB films. The films were deposited in a LB trough (KSV 5000) from a monolayer of arachidic acid (Aldrich, 99% purity) on 0.5-mM cadmium chloride solution at a pressure and temperature 30 m Nm$^{-1}$ and 10 °C, respectively, on silicon wafers. The $p$H was adjusted to 6.5 using sodium bicarbonate. 150 $\mu$l of 1-mg/ml arachidic acid solution in chloroform was spread on cadmium chloride solution to form a monolayer. The silicon wafers were pretreated with an ammonia-peroxide (30%) solution to make it hydrophilic. The dipping speed of the substrate was 3 mm min$^{-1}$ and the drying time between each up-down stroke cycle was 10 min. For our work we have used Milli-Q (Millipore) water with a resistivity of 18.2 M$\Omega$ cm.

The schematic of a typical LB multilayer film, deposited on a hydrophilic substrate, is shown in Fig. 1. Also shown is

the expected electron density profile (EDP), as a function of depth for an ideal film (dashed line) and a film with propagating disorder (solid line), as indicated in the figure. The head corresponds to the hydrophillic part of the amphiphilic molecules [here Cd(COO)$_2$], while the tail corresponds to the hydrophobic part (here [CH$_3$(CH$_2$)$_{18}$]$_2$). X-ray scattering is mainly sensitive to the high-electron-density head region hence the separation between two head regions is detected as the bilayer separation.

The deposited films were subjected to thermal treatment in a sample cell shown schematically in Fig. 2. The cell was made of oxygen-free high-conducting copper for better thermal stability. It consists of two separate parts fitted together with screws. The main part contains an inner copper block on which the sample was mounted along with the temperature sensor which was placed close to the sample. The temperature sensor used was AD-590 (IC temperature transducer) capable of detecting temperature variations in the range $-55$ °C–150 °C. The sensor was calibrated using the data that it produces: a linear current output of 1 $\mu$A/K in the above temperature range. The heater coil (manganin wire) was fitted beneath this copper block. A teflon spacer was used to thermally insulate this inner block from the outer hollow copper block which was mounted on the goniometer (Optix, Microcontrole). In order to monitor the temperature of the surface of the goniometer an LM335 temperature sensor was mounted on the goniometer with a set cutoff temperature to prevent accidental heating of the goniometer. The temperature of the heater was regulated using a home-made proportional-integrator-differentiator (PID) controller. The temperature stability of this controller was found to be $\pm 0.1$ °C. In order to prevent the loss of heat due to convec-

tion, and to prevent a burning out of the film, the sample cell was kept at a pressure of $\simeq 7 \times 10^{-2}$ mbar during the time the films were at high temperature by using a rotary pump with a liquid-nitrogen trap. A kapton x-ray window was used in the sample cell for *in situ* experiments.

X-ray reflectivity and diffuse scattering data was collected using a 18-kW rotating-anode generator (Enraf Nonius, FR591). The x-ray beam was monochromatized using the (111) face of a silicon crystal, and subsequently made to pass through an evacuated flight path before it was incident on collimating slits just before the sample. The slits were used to define the beam size and geometry as well as to select the Cu $K\alpha_1$ component (refer to Fig. 2). The goniometer on which the sample cell and detector were mounted is capable of angular displacements in steps of $0.001°$. Since the direction of the incoming x-ray beam was fixed, the angle of incidence on the sample, mounted on the goniometer, was controlled by changing the angle ($\theta$) of the goniometer head with respect to the beam direction. The scattered beam was taken through an evacuated path, to reduce background scattering and was detected by the NaI scintillation detector mounted on the $2\theta$ arm of the goniometer. The angle of reflection was determined by the angle between the sample surface and the detector. Specular reflectivity measurements were performed by keeping the angle of incidence $\theta_i$ equal to the angle of reflection, $\theta_f$ ($\theta_i = \theta_f = \theta$). Diffuse scattering data were collected in two different modes. The transverse diffuse data were collected by performing rocking scans of the sample, keeping the detector in fixed position ($\theta_i + \theta_f = 2\theta$), while the longitudinal diffuse data were collected by performing a specular scan ($\theta$-$2\theta$ scan) while maintaining a fixed angular offset between $\theta_i$ and $\theta_f$. The incident radiation was collimated by slits having apertures of 100 and 5000 $\mu$m in and perpendicular to the scattering plane, respectively, with the aperture in the scattering plane determining the width of the incident beam in the scattering plane. For specular reflectivity measurements a 400-$\mu$m slit was placed in front of the detector to intercept the total specular component, while in the case of diffuse scattering measurements the reflected beam was defined in the scattering plane by a 100-$\mu$m slit. The aperture perpendicular to the scattering plane before the detector slit was kept wide open, in both cases, to integrate effectively the component of scattering perpendicular to the scattering plane (along $q_y$ in Fig. 2).

The melting experiments were performed on two types of LB films, denoted here as $A$ and $B$, differing in interfacial morphology. These films were prepared by depositing CdA layers on Si(001) substrates having two different miscut angles (low for $A$ and high for $B$). The interfacial morphology of films $A$ and $B$ exhibited logarithmic and self-affine height-height correlation functions[12] respectively. For film $B$ the x-ray data was collected in the sample cell *in situ* as the film was heated in fixed temperature steps. Since it was found that no significant change occurs in the structure of the film between room temperature ($20°C$) and $65°C$ the film was heated directly to $65°C$. After raising the temperature 10 mins time was allowed for the sample to equilibrate to a set temperature before x-ray specular reflectivity data was taken. The temperature was kept fixed while the specular reflectivity data was taken and the temperature stability $\pm 0.1°C$ was ensured by the PID controller. Subsequently

the sample temperature was changed in steps of $5°C$ up to $110°C$. At all temperatures up to $100°C$ the reflectivity data were collected up to $4.45°$ ($\theta$), and was repeated once more to observe the changes, if any, taking place during the time ($\sim 3.5$ h) a particular reflectivity scan was being performed. Significant changes in the specular reflectivity data, during the time of one such scan, were observed only above $95°C$. After taking specular reflectivity data at $100°C$ the film was allowed to cool down to room temperature. Specular reflectivity data of the film were taken again at this temperature. The film was then taken out of the cell, and AFM data were taken in ambient conditions. The film was put back again into the cell and specular reflectivity data was collected again to ensure that no change has taken place in the film during AFM measurements. The off-specular diffuse data were also collected at this stage. After collecting the specular data at $110°C$ the film was allowed to cool down to room temperature before collecting specular and off-specular data. The film was then taken out of the cell again to collect AFM data. Since it was observed that the changes in the film structure as a function of temperature were irreversible and remained essentially the same after cooling down to room temperature the high temperature data for film $A$ was taken *ex situ*. The sample was kept at a fixed temperature under vacuum for 1 h after the particular temperature was attained and then rapidly cooled to room temperature. X-ray specular and diffuse reflectivity and AFM data on the film $A$ were then collected under ambient conditions. All AFM (Park Scientific Instrument) data were collected in contact mode with a silicon nitride cantilever and integrated tip using a 100-$\mu$m piezo scanner. Scans were performed over several areas of the film and at each position several scans of different sizes were taken.

## III. THEORETICAL BACKGROUND

### A. Surface morphology and roughness

Self-affine fractal roughness is commonly observed in a wide variety of physical systems.[20,25] Recently, LB films were also found to exhibit this type of interfacial roughness.[12] For isotropic self-affine rough surfaces the height difference correlation function $g(r)$, can be written

$$g(r) \equiv \langle [z(0) - z(r)]^2 \rangle = Ar^{2\alpha} \quad (0 < \alpha < 1), \quad (1)$$

where $z(r)$ is the height, with respect to a mean surface, at a lateral distance $r$ from some origin where the height is $z(0)$, and $\alpha$ is referred to as the roughness exponent. The exponent $\alpha$ determines the texture of rough surfaces; a lower $\alpha$ indicates a jagged surface, while a higher $\alpha$ implies a surface with relatively smooth fluctuations.[20] All physical systems that we come across exhibit this self-affine scaling only over a finite length scale. If this were not so then the correlation function defined above would diverge, implying that the roughness would grow indefinitely which is an unphysical situation. The length scale up to which self-affine scaling is observed in a surface is called the correlation length. For actual physical systems the form of the height difference correlation function is modified[20] from that given above to

$$g(r) = 2\sigma^2 [1 - \exp(-r/\xi)^{2\alpha}], \quad (2)$$

where $\sigma$ is the rms roughness of the surface, and $\xi$ is the correlation length for self-affine scaling of surface roughness. $g(r)$ can take either of these forms mentioned above depending on the relative magnitude of the length scale, $r$, over which surface roughness is probed and the correlation length $\xi$. Equation (2) above reduces to a form similar to that in Eq. (1) in the limit $r/\xi \ll 1$.

The surfaces of bulk liquids, due to the presence of thermally excited spectrum of capillary waves, exhibit a logarithmic height-height correlation. Recently the surface and interfaces of thin films were also found to exhibit such types of correlation. The height difference correlation function for capillary waves can be written as

$$g(r) = 2\sigma^2 - BK_0(\kappa r), \qquad (3)$$

where $\sigma$ is the true roughness, $K_0$ is the modified Bessel function of the second kind, and $\kappa$ is the lower wave-vector cutoff for capillary waves. LB films have been found to exhibit both self-affine and logarithmic height-height correlations typical of capillary waves. We earlier postulated a general correlation function for multilayer LB films with conformal interfaces as[12]

$$g(r) = \left\{ 2\sigma^2 + B\left[ \gamma_E + \ln\left(\frac{\kappa r}{2}\right) \right] \right\} \{ 1 - \exp[ -(r/\xi)^{2\alpha} ] \}. \qquad (4)$$

Here $\sigma$ is the *true* rms roughness, $\gamma_E$ is the Euler constant, and $\kappa$ is a lower cutoff wave vector ($\sim 10^{-5}$ Å$^{-1}$ here) for logarithmic correlation, $B = k_B T / \pi \gamma$, and $\gamma$ is the interfacial tension. The self-affine and logarithmic correlations, observed in LB films, appear as limiting cases of this general correlation function.

### B. X-ray scattering formalism

The formalism to obtain the scattering cross section of x rays for different types of rough surfaces, characterized by different height difference correlation functions $g(r)$, were discussed in detail.[20] Scattering from a surface can, generally, be separated into two components, namely, specular and diffuse.[9,10,20,21] The specular component arises due to scattering from the average surface, while the diffuse or off-specular component comes from scattering by height fluctuations about this average surface. The specular component is directional, while the diffuse component is distributed around the specular direction. The type of interfacial height-height correlation decides the nature of the distribution of diffusely scattered photons around the specular direction and the ratio of the number of photons scattered in the specular to those in the diffuse directions. In general, for a given incident angle, an increase in the height fluctuation or roughness leads to an increase in the number of photons scattered into the diffuse channels at the expense of the photons scattered in the specular channel, keeping the sum total of the scattered photons the same. In addition to an increase in roughness there may be a decrease in the number of specularly scattered photons due to the variation in electron-density gradients normal to the surface, or interfaces of the system from which scattering is being studied. Such variations do not contribute to the diffuse scattering channels, although a reduction in the number of photons scattered in the specular

channel takes place. In such situations it is often convenient to calculate the diffuse integrated reflectivity, i.e., the total reflectivity after integration over diffuse intensity profile (intensity vs $q_x$) around each point along the specular ridge. By integrating over the diffuse scattering profile the effect of lateral height fluctuations, and hence roughness, in the specular reflectivity is taken care of, and the resulting reflectivity profile depends only on the vertical structure of a system. In this way it is possible to separate out the contribution of roughness and interdiffusion (chemical gradient) in the reflectivity.

The spatial coherence length of the incident x-ray beam decides the region over which information about the nature of surface roughness can be obtained. Since for a true self-affine fractal surface the roughness does not saturate within the coherence length, no true specular component of scattering can be identified, and the total scattering can be regarded as diffuse. This is also true for surfaces with long-range correlation, like logarithmic height correlation without cutoff. The relative magnitude of the correlation length for self-affine scaling of roughness and the coherence length decides the nature of correlation function [Eqs. (1) or (2)], which in turn dictates the nature of the measured scattering profiles. For capillary waves a cutoff for logarithmic correlation also exists, and the nature of the diffuse scattering profile is decided, as in the case of self-affine correlation, by the interplay of beam coherence and this cutoff length.

In most experimental situations the aperture of the detector slit normal to the scattering plane is kept wide open to effectively integrate the component ($q_y$) of scattering normal to the scattering plane. The total scattered intensity for a multilayer system with conformal interfaces and roughness, and with one component of scattering integrated, can be written as[12]

$$I(q_x, q_z) = I_0 \frac{R(q_z) q_z}{2k_0 \sin \theta_i} \times \mathcal{F}(q_x, q_z) \times \mathcal{G}(q_z) + C_0. \qquad (5)$$

Here $R(q_z)$ is the specular reflectivity in the Born approximation, which has been replaced by the reflectivity calculated using Parratt's formalism[19] during data analysis to avoid divergence at low $q_z$ inherent in the Born approximation, $k_0$ ($=2\pi/\lambda$; $\lambda$ is the incident radiation wavelength), $q_z [=k_0(\sin\theta_i + \sin\theta_f)]$ is the component of the wave vector normal to the surface, $q_x [=k_0(\cos\theta_f - \cos\theta_i)]$ is the lateral wave vector component in the scattering plane, and $I_0$ is the direct beam intensity. A constant background $C_0(\simeq 0.04$ counts/sec arising mainly from detector dark current) was added to Eq. (5) for analyzing the experimental data.

The functions $\mathcal{G}(q_z)$ and $\mathcal{F}(q_x, q_z)$ in Eq. (5) depend on the nature of the correlation function $g(r)$. For a perfectly smooth surface $\mathcal{G}(q_z)$ is unity, and $\mathcal{F}(q_x, q_z)$ can be defined as

$$\mathcal{F}_S(q_x, q_z) = \delta q_{xc} \otimes \mathcal{R}(q_x - q_{xc}). \qquad (6)$$

For a system with self-affine fractal height correlation (without cutoff) with exponent $\alpha = 0.5$, $\mathcal{G}(q_z)$ and $\mathcal{F}(q_x, q_z)$ can be defined as

$$\mathcal{G}_{SA}(q_z) = q_z^3 I_{conv}(q_x, q_z)_{q_x=0}, \qquad (7a)$$

$$\mathcal{F}_{SA}(q_x,q_z)=I_{conv}(q_x,q_z)/I_{conv}(q_x,q_z)_{q_x=0}, \quad (7b)$$

where $I_{conv}(q_x,q_z)$ is a resolution convoluted Lorentzian:

$$I_{conv}(q_x,q_z)=\left[\frac{A}{q_{xc}^2+\left[\frac{A}{2}q_z^2\right]^2}\right]\otimes\mathcal{R}(q_x-q_{xc}). \quad (8)$$

Here $q_{xc}$ is a dummy integration variable over which the convolution is performed with respect to the Gaussian resolution function $\mathcal{R}$, centered at $q_x$. The width of the Lorentzian in Eq. (8) depends on $A$ for a fixed $q_z$, and scales with square of $q_z$.

In case of a system with logarithmic height correlation with cutoff, the above functions can be defined as

$$\mathcal{G}_L(q_z)=\exp(-q_z^2\sigma_{eff}^2)\frac{1}{\sqrt{\pi}}\Gamma\left(\frac{1-\eta}{2}\right), \quad (9a)$$

$$\mathcal{F}_L(q_x,q_z)={}_1F_1\left(\frac{1-\eta}{2};\frac{1}{2};\frac{-q_x^2\zeta^2}{4\pi^2}\right), \quad (9b)$$

where ${}_1F_1$ is the Kummer function, $\eta=Bq_z^2/2$, and $\sigma_{eff}$ is the effective interface roughness, as explained earlier.[12,26] The diffuse integrated reflectivity $I_D$ can be defined in general from Eq. (5) as

$$I_D=\int dq_x I(q_x,q_z)$$

$$=I_0\frac{R(q_z)q_z}{2k_0\sin\theta_i}\times\mathcal{G}(q_z)\int dq_x\mathcal{F}(q_x,q_z)$$

$$=I_0\frac{R(q_z)q_z}{2k_0\sin\theta_i}\times\mathcal{G}(q_z)\times\mathcal{F}_D(q_z). \quad (10)$$

Here $\mathcal{F}_D(q_z)=\int dq_x\mathcal{F}(q_x,q_z)$. In specular reflectivity measurements the widths of the detector slits (in our case 400 $\mu$m) are kept much wider than the incident slit (100 $\mu$m here) to intercept the full specular beam, including divergence, and also to effectively integrate over the diffuse component ($q_x$) of scattering. Thus the intensity $I(q_z)$ at the specular position ($q_x=0$) can be written, from Eq. (5), as,

$$I(q_z)=I_0\frac{R(q_z)q_z}{2k_0\sin\theta_i}\times\mathcal{F}_W(q_z)\times\mathcal{G}(q_z), \quad (11)$$

where

$$\mathcal{F}_W(q_z)=\int_{-w}^{+w}dq_x\mathcal{F}(q_x,q_z). \quad (12)$$

Here $w$ is the half-width of the detector aperture used for specular reflectivity measurements, and is indicated in Fig. 3. The quantity that is actually measured experimentally is $I(q_z)$. The diffuse integrated reflectivity $I_D(q_z)$ is related to the experimentally measured reflectivity as,

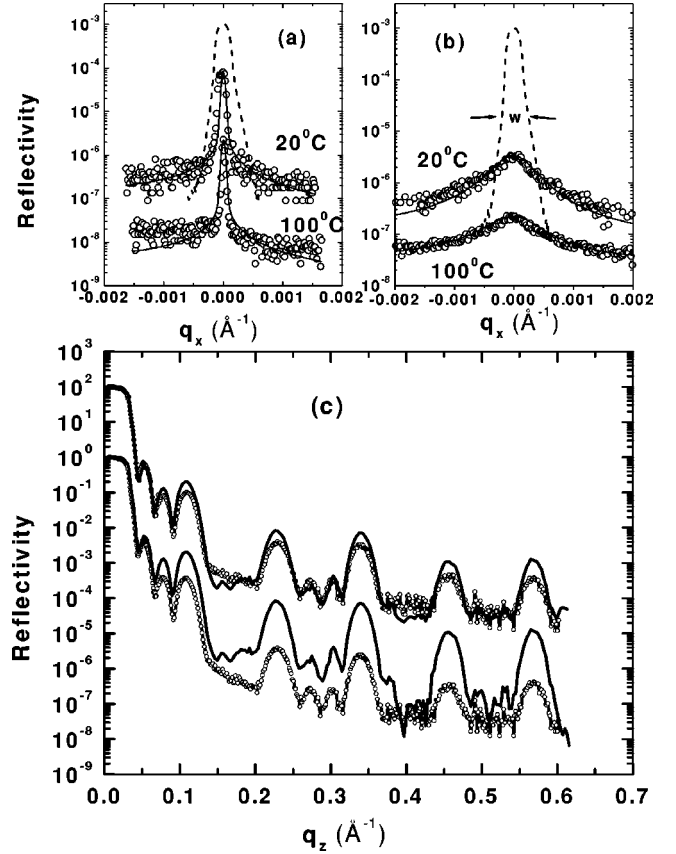$$\frac{I_D(q_z)}{I(q_z)}=\frac{\mathcal{F}_D}{\mathcal{F}_W}=R_S(q_z). \quad (13)$$



FIG. 3. Diffuse scattering data ($\bigcirc$) and fit (solid line) for (a) film $A$ and (b) film $B$ at room temperature (20 °C), and after cooling from 100 °C, all taken at $q_z=0.23$ Å$^{-1}$. The resolution function at this $q_z$ position for 400-$\mu$m detector slits, used for reflectivity measurements, is also shown in both (a) and (b). Note that diffuse data are collected with a 100-$\mu$m detector slit. (c) Experimental specular (lower) and diffuse integrated reflectivity (upper) profiles for films $A$ (solid line) and $B$ ($\bigcirc$) at room temperature. The diffuse integrated profiles have been shifted with respect to the experimental data for clarity.

It is clear from Fig. 3 that for logarithmic correlation $\mathcal{F}_D\simeq\mathcal{F}_W$, but for self-affine correlation $\mathcal{F}_D\gg\mathcal{F}_W$. Hence in our case this scaling of the experimental data was effectively done during experiment for the film with logarithmic interfacial correlation ($A$), while the scaling had to be done numerically for the film with self-affine correlation ($B$). Both $\mathcal{F}_D$ and $\mathcal{F}_W$ were evaluated numerically for the film $B$ from the respective transverse diffuse profiles measured at different $q_z$ values. The value of this ratio was then extrapolated over the entire range of the measured specular reflectivity data and then the reflectivity data at all temperatures for film $B$ were scaled by $R_S(q_z)$ to convert them to the respective diffuse integrated profiles, which is equivalent to reflectivity profiles of zero roughness.

It should be mentioned here that it is possible to extract the roughness exponent of a given surface from the slope of the $\sigma$ vs scan size plot obtained from AFM measurements. On the other hand, by analysis of diffuse scattering line profiles [Eqs. (7) and (9)], one can extract the functional form of the height difference correlation function $g(r)$ and hence the roughness exponent. Statistically, the scaling of rms roughness, $\sigma$ (actually $\sigma^2$) is equivalent to the scaling of
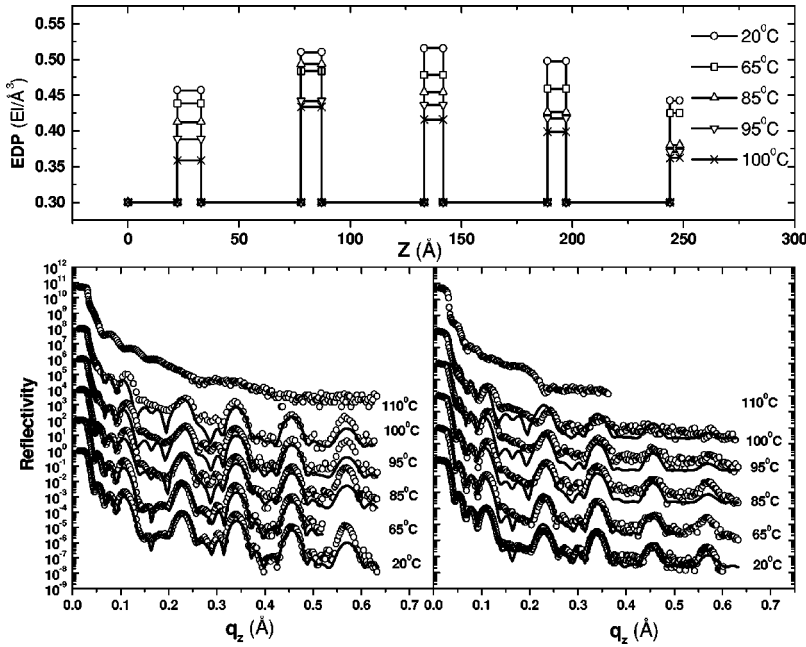
FIG. 4. Obtained electron density profiles (EDP's) at different temperatures for film A (upper panel). The same EDP's were used to match the calculated reflectivity profiles (solid lines) with the respective diffuse integrated profiles (○) for films A (left panel) and B (right panel). Only a scaled background was added to the reflectivity profiles of film B at each temperature (refer to the text). Since no meaningful fit to the data at 110 °C for films A and B could be obtained, we have not presented those calculated profiles. All the profiles were multiplied with respect to their immediate lower curves by a factor of 100 for clarity.

$g(r)$, the height difference correlation function[25] which implies that for a given surface the roughness exponent obtained using AFM and x-ray measurements should be the same.

## IV. EXPERIMENTAL RESULTS

### A. X-ray scattering

The transverse diffuse reflectivity data at room temperature and after cooling to room temperature from 100 °C for both the films are shown in Fig. 3. Only the profiles taken about $q_z = 0.23$ Å$^{-1}$ have been shown here. All the profiles, at room temperature, for film B are best fit by Lorentzians [Eq. (8)], with the widths scaling as $q_z^2$, indicating that the interfaces in the film are self-affine fractals with exponent $\alpha = 0.5$, as was found earlier.[9,12] The profiles of the same film after being cooled from 100 °C are also Lorentzians, the only difference being in the value of the fit parameter A which at room temperature is 0.014 Å and after being cooled from 100 °C is 0.018 Å . This implies that the conformal interfacial roughness exponent $\alpha$ does not change even up to 100 °C. The diffuse reflectivity data at 110 °C is very weak, and hence no meaningful information about the conformal interfacial correlation could be obtained from this data. For film A, the transverse diffuse reflectivity data are fit by Kummer function [Eq. 9(b)], indicating the presence of logarithmic correlation. The only fit parameter[12] is B, which turns out to be 1.6 Å$^2$ for all profiles at room temperature, and at 100 °C again indicating that the correlation of the interfaces remain unchanged up to this temperature. The diffuse data at 110 °C seem to indicate that the conformal interfacial correlation remains unchanged, although a definitive value of the parameter B could not be obtained.

Figure 4 shows the diffuse integrated reflectivity data, and the fitted profiles, at different temperatures for films A and B. Strong Bragg peaks at $q_z = 0.107$, 0.226, 0.339, 0.457 and 0.569 Å$^{-1}$ and well-defined separation between the peaks ($0.115 \pm 0.003$ Å$^{-1}$) are observed in the reflectivity data,

even when the sample is heated up to 85 °C. The presence of strong Kiessig fringes up to 85 °C indicates that the film has more or less uniform thickness (and hence equal number of bilayers) within the coherence length of our x-ray beam. Beyond this temperature the amplitude of the first observable Kiessig fringe ($q_z \simeq 0.05$ Å$^{-1}$) starts to decrease and vanishes totally at 100 °C. This may be an indication that the film thickness becomes inhomogeneous. At 110 °C, the bilayer structure for both the films A and B breaks down completely, as is evident from the disappearance of the bilayer Bragg peaks in the respective x-ray specular reflectivity data. No physically meaningful fit to the 110 °C data could be obtained, and hence the respective fitted profiles were not presented. The general trend in melting seems to be similar for both the films. As discussed earlier, for LB films A, diffuse integration was effectively performed during the experiment (with 400-$\mu$m-detector slits). For films B the experimental reflectivity profile had to be scaled to convert them to the diffuse integrated profiles. The effect of this scaling for the room-temperature reflectivity data of film B is shown in Fig. 3. The lower set of curves are the experimental data for films A and B, while the scaled data are the upper set of curves. The close matching of the two data sets is evident. It may be noted that background counts, 0.04 per secs as mentioned earlier, also increase during this scaling operation of measured reflectivity data for film B. For showing the similarity of the diffuse integrated reflectivity profiles of films A and B an additional constant background has been added to the experimental data on A to account for the effect of background scaling. A similar scaling was also performed on all the data at higher temperatures up to 100 °C.

We have used Eqs. (10) and (13) to perform the scaling of measured reflectivity profiles for films A and B, and $R(q_z)$ was calculated on the basis of a model EDP of films consisting of slices of different thickness, with each slice having a constant average electron density (AED) to carry out the fitting procedure. The thickness of the slices in the high-
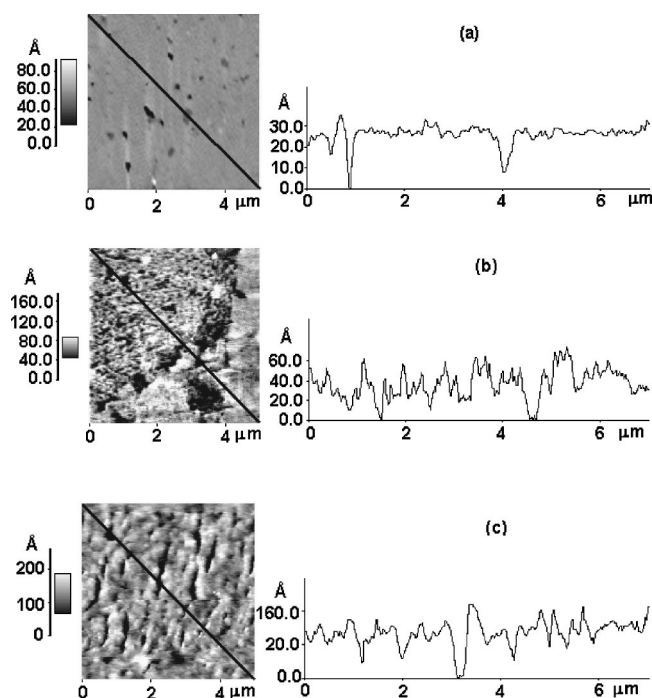
FIG. 5. Atomic force microscopy (AFM) images ($5 \times 5$ $\mu$m$^2$) for film *A*. (a) The as-grown film. (b) After cooling from 100 °C. (c) After cooling from 110 °C. Typical height profiles along the lines drawn on the respective images are also shown side by side.

FIG. 6. Atomic force microscopy (AFM) images ($1 \times 1$ $\mu$m$^2$) for film *B*. (a) The as-grown film. (b) After cooling from 100 °C. (c) After cooling from 110 °C. Typical height profiles along the lines drawn on the respective images are also shown side by side.

electron-density head region was taken to be 5 Å and in the low-electron-density tail region the thickness of each slice was taken to be 50 Å (refer to Fig. 1). The only fit parameters were the AED's of the slices representing the head region, the sizes of all the slices and the AED of the slices representing the hydrocarbon tail region being kept fixed. The tail AED's were fixed at a theoretical value of 0.3 electrons/Å$^3$. Note that we have used a very simplified model for the films, since it brings out the essential features of the melting process. A clear trend of reduction of the density of the head regions with an increase of temperature up to 100 °C is evident from the EDP's obtained at each temperature from an independent fitting of the respective diffuse integrated data for the film *A*. In order to obtain a unified picture of the melting mechanism irrespective of the nature of the interfacial correlation of the films, we used the respective EDP's at each temperature, as obtained for film *A*, to match the diffuse integrated reflectivity profiles at all temperatures for films *B*. Only a scaled background was added to the calculated profiles. The close matching indicates that the mechanism of melting up to 100 °C is independent of the type of interfacial correlation present in the untreated film. The trend of density reduction with temperature could either be due to vertical molecular interdiffusion or due to a lateral expansion of the film. Since diffuse scattering measurements ruled out significant vertical molecular interdiffusion, this trend of density reduction is a signature of lateral motion of molecules, leading to an expansion of the film. Here we have used a much simpler model to extract the same information. A better fit could be obtained with more parameters, but the essential information obtained remains unchanged. At 110 °C, the bilayer structure of the film is destroyed and the film disorders irreversibly. It appears that at this stage gauche
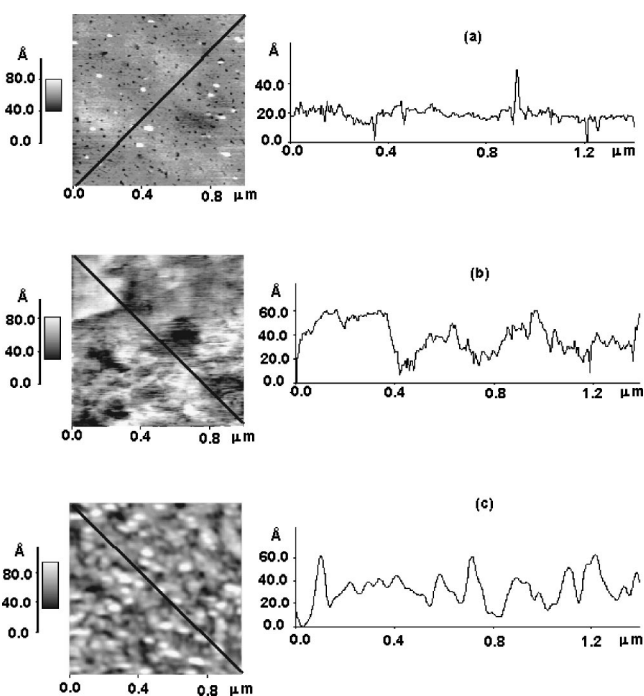
disorder sets into the chains, whereby the chains no longer retain their vertical orientation, leading to destruction of the ordered bilayer structure. Also, since molecular packing is considerably relaxed, interlayer diffusion could become dominant at this temperature.

### B. Atomic force microscopy

AFM images for film *A* before heat treatment (as grown), after being cooled from 100 and 110 °C, are shown in Figs. 5(a), 5(b), and 5(c), respectively. The height profiles drawn beside each topographical image represents the height variation along the line drawn through the respective images, the heights being defined relative to the minimum height along the particular line. The untreated film is very smooth, with only small pinhole defects present. At 100 °C, the film appears to have cracked, with large craters having opened up. As the line profile indicates, the depth of a typical crater is nearly the same as the total film thickness. A similar morphology is also seen for the film at 110 °C, with a noticeably higher defect density as compared to that at 100 °C.

AFM images for film *B* before heat treatment (as grown), after being cooled from 100 and 110 °C, are shown in Figs. 6(a), 6(b), and 6(c), respectively. The height profiles drawn beside each topographical image represent the height variation along the line drawn through the respective images, the heights being defined relative to the minimum height along the particular line. The as-grown film is quite smoothly interspersed with pinhole defects, as can be clearly seen from the typical height profile shown along side the topographical image. After cooling from 100 °C, the film is found to consist predominantly of domains[11] of different heights in the $z$ direction. The typical size of domains is $\sim 0.5$ $\mu$m. Within a
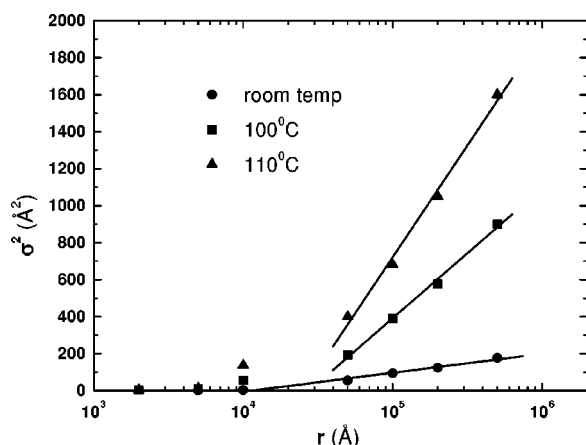
FIG. 7. $\sigma^2$ vs scan length $r$, from AFM images of film $A$ for an untreated film, after cooling from $100°$ and from $110\,°C$. The solid lines are the fits to the linear portion of the respective curves.

domain the film is quite smooth except for the presence of a few defects. The height profile for the film after it is cooled from $100\,°C$ clearly shows that the domain of the largest size in the image (top left corner) presented has a thickness close to the bilayer thickness of the as-grown film. Moreover, the difference in the thickness of the other domains as compared to this domain is small, which explains why appreciable change in bilayer spacing could not be detected from x-ray measurements, even at this temperature, although the thickness inhomogeneity is sufficient to reduce the Kiessig fringe intensity. It is known that the translational correlation length of LB films is $\sim 100$ Å. However, long-range bond orientational order may exist in these films due to a hexatic head group arrangement.[15,17] This in turn produces micron size domains,[15] as observed here. Although the presence of domains is clearly evident in the AFM data at $100\,°C$ (cooled), it is likely that the formation of these domains starts from $90\,°C$ onward, since at this temperature the Kiessig fringes tend to become weaker. After the film is cooled from $110\,°C$ no such smooth domains are visible, and the film becomes rougher, as is evident from the rapid fluctuations in the height profile. It is clear that the smooth large domains that were present in the film at $100\,°C$ (cooled) are absent, and the film becomes disordered at short length scales ($\simeq 100$ Å). This type of morphology is typical of a disordered state, typical of liquids where there is no long range translational or orientational order.

Figure 7 shows the plot of rms roughness $\sigma$ against scan length $r$ for scans of different sizes for the film $A$ at room temperature, after it is cooled to room temperature from 100 and $110\,°C$. The linear fit to the data (log-linear scale) clearly indicates that the correlation at the surface of the film is logarithmic, confirming our earlier observation of the presence of conformal logarithmic interfacial correlation in the film. It is interesting to note that this correlation persists at the surface of the film even up to $110\,°C$, where x-ray reflectivity data indicate that the film has melted. The slope of the linear fit is proportional to the parameter $B$, and the increase of $B$ with temperature is indicative of a decrease in surface tension and hence an increase in roughness. It is difficult to understand whether this is purely a surface effect (as evident from AFM measurements alone) or also takes
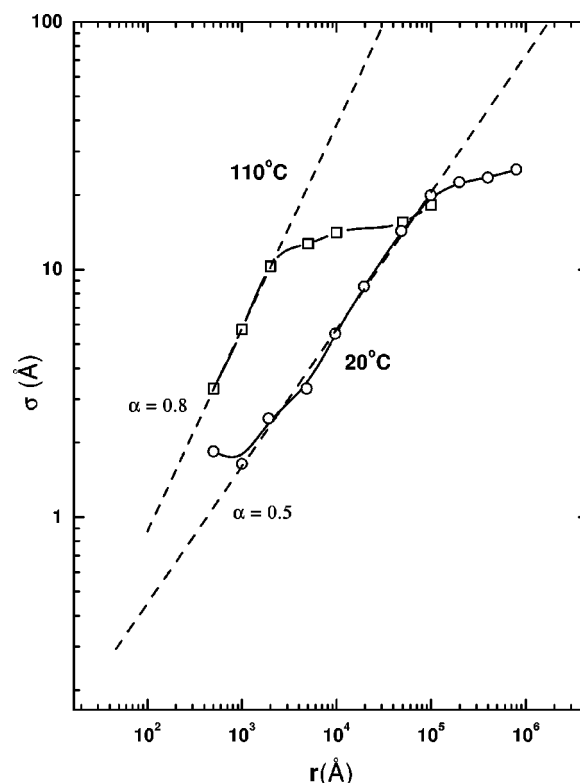


FIG. 8. $\sigma$ vs scan length $r$, from AFM images of film $B$ for an untreated film ($\bigcirc$) and after cooling from $110°$ ($\square$). The dashed lines are fits to the linear portion of the respective curves. Slopes are indicated alongside the respective fits. The solid lines are only a guide to the eye.

place within the film, since this trend cannot be unambiguously confirmed from x-ray diffuse reflectivity at elevated sample temperatures due to low diffuse signal-to-noise ratio inherent in a lab source. We believe, that, due to disorder in the film, the adhesive force between the film and substrate decreases substantially at elevated temperatures, and as a result $B$ increases.

Figure 8 shows the plot of rms roughness $\sigma$ against scan length $r$ for scans of different sizes for film $B$ at room temperature and after it is cooled to room temperature from $110\,°C$. It may be noted that the roughness of both films saturates to a value of about 20 Å beyond the correlation length, as found earlier.[12] The self-affine nature of the films is evident in the log-log plot here. A linear fit to the data shows that the exponent changes from 0.5 to 0.8 as the film undergoes a melting transition. The correlation lengths for as-grown and melted films were found to be $\simeq 15$ and $\simeq 0.1$ $\mu$m, respectively, as is clearly indicated by the limits of the linear fits. This length for as-grown film is beyond the coherence length of our x-ray beam ($\simeq 10$ $\mu$m here), and hence in x-ray measurements the film appears to have no cutoff.[12]

In conclusion, analysis of x-ray reflectivity, diffuse scattering, and AFM data on LB films of cadmium arachidate with two different types of in-plane height-height correlation, self-affine and logarithmic, suggest that melting of the film occur predominantly through the lateral motion of molecules. Here we have also developed a diffuse integrated reflectivity data analysis scheme to extract electron density profile as a function of depth that is independent of in-plane correlation present at the interfaces. Our results suggest that

the LB film does not behave strictly as a 2D system, since the interlayer coupling is important in deciding the melting behavior. A more detailed study with finer temperature steps is in progress to understand the mechanism of melting very close to the bulk melting point of LB films.

---

[1] G. L. Gaines, Jr., *Insoluble Monolayers at the Gas-Liquid Interface* (Wiley, New York, 1966).

[2] V. M. Kaganer, H. Mohwald, and P. Dutta, Rev. Mod. Phys. **71**, 779 (1999).

[3] V. M. Kaganer and E. B. Loginov, Phys. Rev. Lett. **71**, 2599 (1993).

[4] M. K. Durbin, A. G. Richter, C.-J. Yu, J. Kmetko, J. M. Bai, and P. Dutta, Phys. Rev. E **58**, 7686 (1998).

[5] J. Als-Nielsen, D. Jacquemann, K. Kjaer, F. Leveiller, M. Lahav, and L. Leseirowitz, Phys. Rep. **246**, 251 (1994); A. Datta, M. K. Sanyal, A. Dhanabalan, and S. S. Major, J. Phys. Chem. B **101**, 9280 (1997).

[6] D. K. Schwartz, Surf. Sci. Rep. **27**, 241 (1997).

[7] J. Zasadzinski *et al.*, Science **263**, 1726 (1994).

[8] J. K. Basu and M. K. Sanyal, Phys. Rev. Lett. **79**, 4617 (1997).

[9] A. Gibaud *et al.*, Phys. Rev. Lett. **74**, 3205 (1995).

[10] V. Nitz *et al.*, Phys. Rev. B **54**, 5038 (1996).

[11] R. Stömmer and U. Pietsch, J. Phys. D **29**, 3161 (1996); R. Stömmer *et al.*, Physica B **221**, 284 (1996); U. Englisch *et al.*, *ibid.* **248**, 258 (1998); S. Vitta *et al.*, J. Chem. Phys. **111**, 11088 (1999).

[12] J. K. Basu, S. Hazra, and M. K. Sanyal, Phys. Rev. Lett. **82**, 4675 (1999).

[13] J. M. Kosterlitz and D. J. Thouless, J. Phys. C **6**, 1181 (1973); D. R. Nelson and B. I. Halperin, Phys. Rev. B **19**, 2457 (1979); A.

P. Young, *ibid.* **19**, 1855 (1979).

[14] J. P. Rabe, J. D. Swalen, and J. F. Rabolt, J. Chem. Phys. **86**, 1601 (1987); Y. Sasanuma, Y. Kitano, A. Ishitani, H. Nakahara, and K. Fukuda, Thin Solid Films **199**, 359 (1991); T. R. Vierheller *et al.*, Langmuir **12**, 5156 (1996).

[15] J. E. Riegler, J. Phys. Chem. **93**, 6475 (1989).

[16] W. Richardson and J. K. Blasie, Phys. Rev. B **39**, 12165 (1989).

[17] H. D. Sikes and D. K. Schwartz, Science **278**, 1604 (1997); M. P. Fontana and P. Facci, J. Chem. Phys. **111**, 5562 (1999).

[18] S. Ostlund and B. I. Halperin, Phys. Rev. B **23**, 335 (1981).

[19] L. G. Parratt, Phys. Rev. **95**, 359 (1954).

[20] S. K. Sinha, E. B. Sirota, S. Garoff, and H. B. Stanley, Phys. Rev. B **38**, 2297 (1988).

[21] M. K. Sanyal, Radiat. Phys. Chem. **51**, 487 (1998).

[22] V. Hóly and T. Baumbach, Phys. Rev. B **49**, 10 668 (1994).

[23] M. K. Sanyal, S. K. Sinha, A. Gibaud, S. K. Satija, C. F. Majkrzak, and H. Homma, in *Applications of Synchrotron Radiation to Materials Science III*, edited by L. Terminello, S. Mini, D. L. Perry, and H. Ade, MRS Symposia Proceedings No. 437 (Materials Research Society, Pittsburgh, 1995), p. 73.

[24] J. A. DeRose and R. M. Leblanc, Surf. Sci. Rep. **22**, 73 (1995).

[25] A.-L. Barabasi and H. E. Stanley, *Fractal Concepts in Surface Growth* (Cambridge University Press, New York, 1995).

[26] M. K. Sanyal, S. K. Sinha, K. G. Huang, and B. Ocko, Phys. Rev. Lett. **66**, 628 (1991).